Research Square

Preprints are preliminary reports that have not undergone peer review.
They should not be considered conclusive, used to inform clinical practice,
or referenced by the media as validated information.

Long-term axial tissue remodeling following posterior lumbar ligament complex injury in SKG mice

Yue Chen
Chengdu Bio-HT Company Limited
Dan Su
Chengdu Bio-HT Company Limited
Feng Luo
Chengdu Bio-HT Company Limited
Min Zhang
Chengdu Bio-HT Company Limited
Yuwei Xu
Chengdu Bio-HT Company Limited
Xiaorong Sun
xiaorong.sun@bio-ht.cn
Chengdu Bio-HT Company Limited

Research Article

Keywords: Ligament injury, Enthesis, Tissue remodeling, Fibrosis, Fibrocartilage, SKG mice

Posted Date: November 12th, 2026

DOI: https://doi.org/10.21203/rs.3.rs-11429294/v1

License: This work is licensed under a Creative Commons Attribution 4.0 International License.
Read Full License

Additional Declarations: No competing interests reported.

Abstract

Background

Local injury may contribute to persistent remodeling of spinal ligament-associated tissues. We examined long-term axial tissue changes after posterior lumbar ligament complex injury in autoimmune-prone SKG mice, using curdlan-treated mice as a comparator with peripheral inflammatory manifestations.

Methods

Thirteen male SKG mice were allocated to Control (n = 3), curdlan (n = 5), or structural injury (n = 5) groups and followed for 15 months. Control mice received no pharmacological or surgical intervention. Monthly clinical and rotarod assessments and serial micro-computed tomography were complemented by terminal histology, immunofluorescence, and serum cytokine measurements in the two intervention groups. Endpoint comparisons used two-sided exhaustive permutation tests of the Mann–Whitney statistic, with Holm adjustment for defined imaging and histology families. Longitudinal outcomes were summarized descriptively.

Results

Curdlan-treated mice developed sustained peripheral arthritis. Posterior lumbar total histology scores were higher after injury than after curdlan treatment (median 6 versus 0; Holm-adjusted p = 0.0476). Fibrosis, fibrocartilage metaplasia, and new bone/bridging-tendency scores were also higher (adjusted p = 0.0397 for each domain). Sacroiliac total histology scores were higher (median 5 versus 1; adjusted p = 0.0476), although individual sacroiliac domains and regional micro-computed tomography scores did not differ after adjustment. Exploratory serum analysis showed higher interleukin-23 after injury (nominal p = 0.0079).

Conclusions

Posterior lumbar ligament complex injury was associated with long-term axial tissue remodeling in SKG mice, with the clearest histological differences in the posterior lumbar region. These observations support further investigation of injury-associated remodeling and its relationship to inflammation and repair. They do not establish a validated model of axial spondyloarthritis or a specific effect of autoimmune susceptibility.

Background

Ligament–bone interfaces transmit load while accommodating inflammation, matrix turnover, and tissue repair. Experimental studies established that mechanical strain can influence entheseal inflammation

and new bone formation through local stromal responses [1]. More recent work showed that mechanical loading can determine the anatomical localization of inflammation and erosive damage through mesenchymal-cell chemokine production [2]. Studies of tenascin-C and Piezo1 have further connected extracellular-matrix adhesion and mechanotransduction to entheseal chondrogenesis and pathological bone formation [3, 4]. Together, these findings provide a rationale for investigating the long-term consequences of spinal ligament-associated injury.

The enthesis also contains resident cells capable of regulating local immune responses. Human spinal entheseal myeloid cells can produce interleukin (IL)-23 and tumor necrosis factor (TNF) following stimulation [5], while resident γδ T-cell subsets exhibit inducible IL-17A production with differing relationships to IL-23 receptor expression [6]. Recent functional studies identified a CD39/CD73-dependent immunoregulatory role for entheseal stromal cells [7]. These observations suggest that local tissue conditions may shape inflammatory responses and repair.

Persistent remodeling after injury also warrants consideration outside disease-specific models. In experimental heterotopic ossification, elevated transforming growth factor beta (TGF-β) activity and injury-associated monocyte/macrophage responses can promote osteochondrogenic differentiation [8, 9]. Lineage studies have identified CD26-positive tendon progenitor cells that contribute to both repair and heterotopic bone formation [10]. These studies illustrate how repair and abnormal tissue differentiation can share cellular components. They do not imply that fibrosis or fibrocartilage observed after spinal surgery necessarily represents heterotopic ossification or spondyloarthritis.

SKG mice carry a Zap70 mutation that alters T-cell selection and confers susceptibility to autoimmune arthritis [11]. Curdlan exposure can produce inflammatory musculoskeletal manifestations in this strain, including enthesitis and axial involvement [12]. IL-23-dependent responses and interactions with the intestinal microbiota contribute to the phenotype [13, 14]. Nevertheless, treatment assignment alone does not establish the anatomical distribution or severity of pathology in a particular cohort. Peripheral arthritis cannot substitute for direct evidence of axial ankylosis.

Recent studies using curdlan-treated SKG mice have investigated platelet-derived growth factor B (PDGFB) and its receptor PDGFRB, hypoxia-inducible factor-1 alpha (HIF-1α) and macrophage migration inhibitory factor (MIF), and osteoclast-derived dipeptidyl peptidase-4 (DPP4) in musculoskeletal inflammation and remodeling [15, 16, 17]. These interventions demonstrate the value of the model for examining specific biological questions. A different question is whether disruption of posterior lumbar ligament-associated tissues in the same genetic background is followed by persistent tissue remodeling over a prolonged observation period.

We therefore conducted an exploratory study of axial tissue changes 15 months after posterior lumbar ligament complex injury in SKG mice. Curdlan-treated mice provided an immune-stimulated comparator, while untreated Control mice provided longitudinal clinical, functional, and imaging reference observations. Clinical assessment and micro-computed tomography were combined with terminal histology, collagen measurements, spatial immunofluorescence, and serum cytokine assessment.

Methods

Animals and study design

Thirteen male SKG mice were obtained from GemPharmatech Co., Ltd. (China) at 6–8 weeks of age and 18–25 g body weight. Mice underwent 1 week of acclimatization before the experiment. They were housed under specific pathogen-free conditions at 20–25 °C and 60% ± 10% relative humidity, with a 12-h light/dark cycle and unrestricted access to food and water. Genotype was assessed by mutation-specific polymerase chain reaction of ear or toe DNA, agarose-gel electrophoresis, and Sanger sequencing of the Zap70 W163C locus. Positive, C57BL/6 genomic-DNA negative, and no-template controls were included. All study animals were homozygous for the expected mutation.

Mice were randomly allocated to Control (n = 3), curdlan (n = 5), and structural injury (n = 5) groups, taking baseline body weight into account. Control mice received no drug or surgical intervention. Follow-up continued for 15 months. The animal was the experimental and statistical unit. All three groups contributed clinical, functional, and micro-computed tomography observations; terminal histology, immunofluorescence, and serum analyses compared the two intervention groups (Table 1). Curdlan and structural injury animals were identified as C1–C5 and AS1–AS5, respectively.

All animal procedures were approved by the Institutional Animal Care and Use Committee of Chengdu Bio-HT Company Limited (approval no. 2022IINC24R20) and conducted in accordance with the Chinese Guidelines for the Ethical Review of Laboratory Animal Welfare. Reporting was organized with reference to ARRIVE 2.0 [18].

Posterior lumbar injury and curdlan administration

Under isoflurane anesthesia, a posterior midline incision was made over L2–L6. The supraspinous and interspinous ligaments, adjacent paraspinal soft tissues, and posterior ligament-associated structures were sharply disrupted while preserving vertebral bone and spinal canal contents. The wound was closed in layers. Meloxicam was administered subcutaneously at 4 mg/kg once daily for 3 days, with routine postoperative monitoring and care. The intervention is termed posterior lumbar ligament complex injury because it involved several associated soft-tissue structures rather than an isolated enthesis.

The curdlan group received 3 mg curdlan (Sigma-Aldrich; cat. C7821-5G) by intraperitoneal injection on days 0 and 7. Published SKG studies provide the biological context for this immune-stimulation approach [12,13]. The curdlan group served as an intervention comparato.

Clinical observations and rotarod testing

Body weight, general condition, and peripheral joint manifestations were assessed monthly from month 0 to month 15. Three observers blinded to group allocation scored peripheral arthritis, and their mean was used as the animal-level score. Longitudinal outcomes were summarized using the available group means, standard deviations, and standard errors.

Rotarod performance was assessed monthly using an SA102 apparatus (Jiangsu Saiangsi Biotechnology Co., Ltd., China). Adaptation comprised 10 r/min for 2 min followed by 30 r/min for 3 min. Mice then completed three training trials starting at 4 r/min and accelerating to 40 r/min over a maximum of 5 min, with at least 15 min between trials. During testing, rotation started at 4 r/min and accelerated at the reported rate of 10 r/min² toward a maximum of 60 r/min. Latency to fall was recorded with a 5-min cutoff. Foam padding was placed beneath the apparatus, and records were evaluated with group allocation concealed. Rotarod latency was treated as a general functional outcome.

Micro computed tomography

In vivo whole-body micro-computed tomography (micro-CT) was performed at months 5, 10, and 15 using a Quantum GX system (PerkinElmer, USA). Sagittal, coronal, and axial reconstructions and three-dimensional views were generated. Serial images were used for descriptive assessment; quantitative group comparisons used the available endpoint regional scores.

Erosion, sclerosis, osteophyte/enthesophyte formation, and bridging/ankylosis-like change were each graded from 0 to 3 in the sacroiliac joints (SIJs), paws/peripheral small joints, and caudal vertebrae, giving regional totals of 0–12. SIJ scores were bilateral means; paw and tail scores used the highest reproducible grade within each defined region. Lesions were assessed on multiplanar images with attention to motion, segmentation, and partial-volume artifacts. Image datasets were coded and scored with group allocation concealed. Posterior lumbar reconstructions were evaluated qualitatively and were not included in the regional composites. Detailed criteria and aggregation rules are provided in Additional file 2, Table S1.

Terminal sampling and serum cytokines

At month 15, mice were euthanized by sodium pentobarbital overdose (150 mg/kg). Terminal blood was collected under deep anesthesia before tissue harvest, and death was confirmed before collection of SIJ and posterior lumbar tissues. Serum IL-17A, IL-23, IL-6, and tumor necrosis factor alpha (TNF-α) were measured in the curdlan and structural injury groups using mouse ELISA kits from MultiSciences (Lianke) Biotech, China (cat. EK217/2-96, EK223/2-96, EK206/2-96, and EK282HS/2-96, respectively), according to the manufacturer's instructions. Plates were processed using a Rayto automated washer and read with a BioTek microplate reader.

Two curdlan-group IL-17A observations were recorded as below detection (ND). For rank-based comparison, these observations were tied below all quantified values; the numerical sentinel used for ordering was not treated as a measured concentration. ND observations were displayed at the lower plotting boundary.

Histology and collagen quantification

SIJ and L3–L4 posterior lumbar specimens from the two intervention groups were fixed, processed for serial sectioning, and stained with hematoxylin and eosin (H&E), Masson trichrome, and Safranin O/Fast Green. Five domains were scored from 0 to 3 at each site. SIJ domains were inflammation, cartilage matrix loss, erosion, fibrous/fibrocartilaginous bridging, and osseous bridging/ankylosis-like change. Posterior lumbar domains were ligament damage/scar replacement, enthesitis/periostitis, fibrosis, fibrocartilage metaplasia, and new bone/bridging tendency. Sections were coded for blinded assessment, and observations were aggregated within each animal.

Site totals, combined totals, and study-specific structural indices were calculated as defined in Additional file 2, Table S2. These indices were treated as exploratory composites rather than validated measures of disease severity or fusion. H&E tissue-area fraction was assessed against the 80% evaluability threshold specified in the scoring documentation. Tissue coverage was considered separately from other aspects of image quality.

Collagen-positive area was quantified within scar-like, entheseal-remodeling, and paraspinal interstitial regions, excluding bone and the normal dense collagen core of intact ligament. Final ROI-restricted percentages were used for the main collagen comparison. Automated whole-tissue fractions represent a different measurement definition and were retained separately as a sensitivity analysis (Additional file 2, Table S3). The two sets of measurements were neither pooled nor substituted for one another.

Exploratory immunofluorescence

SIJ and posterior lumbar sections underwent dual immunofluorescence staining for TNF-α (clone MP6-XT22, cat. 11-7321-82; Thermo Fisher Scientific) and bone morphogenetic protein 2 (BMP-2; cat. PA5-85956; Thermo Fisher Scientific). Imaging used a Nikon ECLIPSE C1 microscope and Pannoramic MIDI whole-slide scanner (3DHISTECH). Nine anatomically defined regions of interest (ROIs) were evaluated per tissue using SaiViewer. Tissue edges, folds, empty spaces, and marked nonspecific autofluorescence were excluded. Images were coded before analysis, with group allocation concealed. ROI definitions and calculation rules are provided in Additional files 1 and 2.

Positive-signal densities were calculated by dividing TNF-α-positive, BMP-2-positive, or double-positive counts by evaluable ROI area. Animal-level tissue summaries were unweighted means across the nine ROIs. One curdlan SIJ specimen was unavailable because of severe section detachment and incomplete

tissue representation after repeated staining; SIJ analyses therefore included four curdlan and five structural injury specimens, and posterior lumbar analyses included five per group. The reported immunofluorescence analyses were restricted to densities.

Statistical analysis

Endpoint analyses were conducted in Python using NumPy and SciPy [19]. Two-sided permutation p values for the Mann–Whitney U statistic were obtained by exhaustively enumerating group-label assignments while retaining tied ranks. The two-sided p value was twice the smaller inclusive tail probability, capped at one. Calculations were cross-checked using an independent SciPy permutation implementation.

Holm correction was applied to the three pairwise group comparisons within each micro-CT region and endpoint. Histological families comprised six summary endpoints, all five SIJ domains, all five posterior lumbar domains, two ROI-restricted Masson site comparisons, and two H&E evaluability comparisons. The complete five-domain correction was retained when selected domains were displayed in the main figure. Automated whole-tissue collagen fractions were analyzed as a separate two-site sensitivity family.

Endpoint data are presented as individual animal observations and medians with interquartile ranges. Cliff's delta is positive when values are higher in the structural injury group than in the curdlan group. Longitudinal outcomes are presented as means ± standard error.

Use of generative artificial intelligence

OpenAI ChatGPT assisted with English-language editing. The authors retain responsibility for the data, analysis, references, interpretation, and final submitted content.

Results

Longitudinal clinical and functional observations

Curdlan-treated mice showed sustained peripheral arthritis during follow-up (Fig. 1). At month 15, mean peripheral arthritis scores were 5.94 in the curdlan group, 0.68 in the structural injury group, and 0 in the Control group. These observations characterize the peripheral inflammatory phenotype of the curdlan group in this cohort.

Mean body weights at month 15 were 26.22, 28.92, and 32.00 g in the curdlan, structural injury, and Control groups, respectively. Mean rotarod latencies differed at baseline (21.14, 28.32, and 46.47 s, respectively) and were 8.44, 5.68, and 31.67 s at month 15. These descriptive trajectories should be

interpreted in light of baseline functional imbalance and the effects of aging, peripheral disease, and general health on rotarod performance.

Endpoint micro computed tomography findings

Representative micro-CT reconstructions illustrated variation in axial configuration and regional skeletal morphology (Fig. 2). Endpoint median SIJ total scores were 0, 1, and 6 in the Control, curdlan, and structural injury groups, respectively. Corresponding paw total scores were 0, 3, and 3, and tail total scores were 0, 3, and 3. No regional total-score or domain-level pairwise comparison reached significance after the defined Holm corrections (all adjusted $p \geq 0.1071$; Figure S2 and Additional file 3).

Axial histology showed greater posterior lumbar remodeling scores after injury

Terminal histological analysis compared the two intervention groups (Fig. 3 and Table S3). SIJ total scores were 5 [4–6] after injury versus 1 [1–1] after curdlan treatment; posterior lumbar totals were 6 [5–9] versus 0 [0–1]; and combined totals were 11 [11–13] versus 1 [1–2] (median [interquartile range]). Each comparison had a Holm-adjusted p value of 0.0476 within the six-endpoint summary family and Cliff's delta of 1.00.

Within the complete posterior lumbar five-domain family, fibrosis, fibrocartilage metaplasia, and new bone/bridging-tendency scores were higher after injury (adjusted $p = 0.0397$ and Cliff's delta = 1.00 for each domain). Enthesitis/periostitis and ligament damage/scar replacement did not reach the adjusted threshold ($p = 0.0952$ and 0.2381, respectively). No individual SIJ domain reached significance after five-domain correction ($p = 0.1587$–1.0000; Figure S3). The clearest domain-level differences thus concerned posterior lumbar remodeling.

Posterior lumbar and combined structural indices were higher in the structural injury group (adjusted $p = 0.0476$ for each), whereas the SIJ structural index was not significantly different ($p = 0.1349$). As composites of the scored domains, these indices summarize the same tissue observations and do not provide independent evidence of fusion.

Posterior lumbar ROI-restricted collagen-positive area was 37.0% [36.9–40.6] after injury versus 28.2% [22.8–32.5] after curdlan treatment ($p = 0.0159$). SIJ values were 31.3% [25.5–38.0] versus 23.0% [23.0–29.8], respectively ($p = 0.0873$). Automated whole-tissue fractions are reported separately in Table S3. All included H&E tissue-area fractions exceeded the 80% evaluability criterion (Figure S3).

Exploratory TNF-α and BMP-2 immunofluorescence

At the SIJ, median BMP-2-positive signal density was 3849.8/mm² in the structural injury group and 1505.6/mm² in the curdlan group (nominal $p = 0.0317$). TNF-α-positive and double-positive densities were not significantly different (nominal $p = 0.2857$ and 0.7302, respectively). In posterior lumbar tissue, TNF-α-positive density was lower after injury (432.7 versus 1973.8/mm²; nominal $p = 0.0317$). BMP-2-

positive density was numerically higher (2969.2 versus 698.1/mm²; nominal p = 0.1508), while double-positive density did not differ (nominal p = 1.0000). These exploratory comparisons are shown in Fig. 4, with anatomical templates, regional densities, and single-channel images in Figures S1, S4, and S5, respectively.

Terminal serum cytokines

Serum IL-23 was higher in the structural injury group than in the curdlan group (38.59 [18.47–45.93] versus 1.23 [0.94–3.68] pg/mL; nominal p = 0.0079; Fig. 5). IL-17A did not reach the nominal significance threshold (p = 0.0556; two curdlan observations were ND). IL-6 and TNF-α comparisons were also non-significant (p = 0.0952 and 0.3095, respectively).

Discussion

The principal finding was a long-term axial histological remodeling phenotype after posterior lumbar ligament complex injury in SKG mice. The clearest domain-level differences relative to curdlan treatment involved posterior lumbar fibrosis, fibrocartilage metaplasia, and new bone/bridging tendency. Histological totals were higher at both axial sites, but individual SIJ domains and regional micro-CT comparisons were less conclusive after multiplicity adjustment. The study therefore supports a tissue-remodeling phenotype more strongly than it supports established axial ankylosis.

The posterior lumbar findings are biologically compatible with a prolonged response to local tissue disruption. Mechanical strain can influence entheseal pathology and local chemokine production [1, 2], while tenascin-C and Piezo1 can link matrix properties and force sensing to osteochondral differentiation [3, 4]. Injury to supraspinous, interspinous, and adjacent paraspinal tissues could plausibly alter load transmission and initiate sustained repair. However, neither mechanical loading nor these pathways was measured here.

In a related study from our group, posterior L2–L6 musculoligamentous injury in rhesus macaques was followed for up to 50 months using serial CT/MRI, ex vivo micro-CT, and whole-section histology [20]. The reported phenotype included posterior ossification and bridging, with late sacroiliac fusion, and histology supported fibrotic and fibro-osseous remodeling. This study provides relevant comparative context for the posterior remodeling observed here. However, species, observation period, operative details, and control design limit direct extrapolation: the macaque study included sham-operated controls, whereas the present study compared terminal tissues from injured and curdlan-treated SKG mice. The present mouse findings therefore do not establish an equivalent ankylosis phenotype or a shared temporal or molecular mechanism.

Human spinal-ligament studies have implicated chondrogenesis and subsequent mineralization in ankylosing spondylitis-associated ossification [21]. In other injury models, TGF-β-dependent progenitor recruitment, monocyte/macrophage responses, and tendon-resident progenitor differentiation contribute to ectopic bone formation [8, 9, 10]. Local lymphatic regulation can also modify the inflammatory

environment and heterotopic ossification after tendon injury [22]. These studies identify plausible processes for future investigation, but the present endpoint sections cannot reconstruct a sequence from fibrosis through fibrocartilage to mature bone. Collagen accumulation and a new bone/bridging-tendency score should therefore not be treated as proof of that sequence or of complete fusion.

The curdlan group developed sustained peripheral arthritis and provided a comparison within the same genetic background. Published SKG studies have demonstrated axial inflammation and investigated PDGFB, HIF-1α/MIF, and DPP4-related remodeling [12, 15, 16, 17]. Nevertheless, protocol, tissue, and observation-period differences limit direct comparisons across studies. Lim and colleagues found that TNF inhibition reduced spinal inflammation in curdlan-treated SKG mice without a corresponding reduction in the measured spinal osteoblast activity [23]. This distinction also cautions against equating any one inflammatory or imaging measure with structural progression. Our results compare outcomes after different interventions; they do not rank the fidelity of two ankylosing spondylitis models.

Exploratory immunofluorescence showed higher SIJ BMP-2-positive density and lower posterior lumbar TNF-α-positive density after injury, while other density comparisons were inconclusive. Human enthesis studies demonstrate both inducible myeloid cytokine production and stromal immunoregulation [5, 7], and work on TNF-α–ELMO1 signaling shows that inflammatory stimulation can influence mesenchymal-cell migration in ankylosing spondylitis [24]. These findings illustrate why marker distributions cannot be reduced to a binary division between inflammation and repair. Our staining did not establish cell lineage, pathway activity, or temporal order. BMP-2-positive signal density is not a direct measure of osteoblast number, and co-occurrence of staining does not establish molecular interaction.

Terminal serum IL-23 was higher in the injury group, which argues against interpreting surgery as a non-inflammatory intervention. Experimental HLA-B27-transgenic rat studies found different requirements for IL-23 signaling during initiation and persistence of disease [25]; human entheseal γδ T-cell studies likewise identify differences in IL-23 receptor-associated cytokine responses [6]. These observations concern distinct systems, but they emphasize the importance of timing and cellular context. A single late serum measurement cannot identify the inflammatory history of a tissue lesion, and nominal cytokine comparisons remain exploratory.

Several limitations constrain inference. The groups were small and unequal, limiting precision. Control mice did not contribute terminal tissue or serum measurements, restricting assessment against normal aging. Rotarod performance differed at baseline and is influenced by peripheral disease and general health. Longitudinal analyses were descriptive because individual repeated observations were unavailable in the analysis dataset; quantitative micro-CT comparisons were limited to endpoint regional scores. Histological criteria and weighted indices were study-specific, and inter-rater reliability estimates were unavailable. Collagen fractions depend on ROI definition and are not interchangeable with whole-tissue estimates. Multiple exploratory serum and immunofluorescence comparisons increase the risk of chance findings. These limitations favor focused replication over broad mechanistic or disease-model claims.

The prolonged observation period provides a basis for testing whether an injury-associated tissue response persists and how it evolves. A confirmatory design should include sham surgery, untreated terminal tissue controls, and an injury group on a non-autoimmune background, with a prespecified primary outcome and justified sample size. Serial quantitative imaging and early and late tissue sampling could then distinguish scar formation, fibrocartilage differentiation, inflammatory persistence, and ossification. Perturbation of candidate pathways would be required to move from the associations observed here to a mechanistic explanation.

Conclusions

Posterior lumbar ligament complex injury in SKG mice was associated with long-term axial tissue remodeling, particularly higher posterior lumbar fibrosis, fibrocartilage metaplasia, and new bone/bridging-tendency scores relative to curdlan-treated mice. The findings support further study of injury-associated tissue responses in this genetic background. They do not establish definite axial ankylosis, independence from inflammation, or a specific contribution of autoimmune susceptibility.

Abbreviations

BMP-2, bone morphogenetic protein 2; CD, cluster of differentiation; DPP4, dipeptidyl peptidase-4; ELISA, enzyme-linked immunosorbent assay; H&E, hematoxylin and eosin; HIF-1α, hypoxia-inducible factor-1 alpha; IF, immunofluorescence; IL, interleukin; MIF, macrophage migration inhibitory factor; micro-CT, micro-computed tomography; ND, below detection; PDGFB, platelet-derived growth factor B; PDGFRB, platelet-derived growth factor receptor beta; ROI, region of interest; SIJ, sacroiliac joint; TGF-β, transforming growth factor beta; TNF-α, tumor necrosis factor alpha.

Declarations

Ethics approval and consent to participate

Animal procedures were approved by the Institutional Animal Care and Use Committee of Chengdu Bio-HT Company Limited (approval no. 2022IINC24R20) and conducted in accordance with the Chinese Guidelines for the Ethical Review of Laboratory Animal Welfare. Consent to participate is not applicable to this laboratory animal study.

Clinical trial number

Not applicable.

Consent for publication

Not applicable.

Availability of data and materials

Animal-level endpoint measurements, longitudinal group summaries, ROI counts and areas, and statistical results supporting this article are included in Additional file 3. ROI-restricted and automated whole-tissue collagen measurements are identified separately. The complete original imaging datasets and other underlying experimental records are not included in the supplementary workbook and are available from the corresponding author on reasonable request.

Competing interests

The authors are affiliated with Chengdu Bio-HT Company Limited, as indicated in the author information. The authors declare no other competing interests.

Funding

This research received no specific grant from funding agencies in the public, commercial, or not-for-profit sectors.

Authors' contributions

YC contributed to conceptualization, supervision, data curation, and writing the original draft and revisions. DS contributed to visualization, supervision, and resources. FL contributed to data curation, visualization, and resources. MZ contributed to data curation and investigation. YX contributed to investigation and visualization. XS contributed to conceptualization, data curation, and writing the original draft and revisions.

Acknowledgements

Not applicable.

References

1. Jacques P, Lambrecht S, Verheugen E, Pauwels E, Kollias G, Armaka M, et al. Proof of concept: enthesitis and new bone formation in spondyloarthritis are driven by mechanical strain and stromal cells. Ann Rheum Dis. 2014;73:437–45. 10.1136/annrheumdis-2013-203643.
2. Cambré I, Gaublomme D, Burssens A, Jacques P, Schryvers N, De Muynck A, et al. Mechanical strain determines the site-specific localization of inflammation and tissue damage in arthritis. Nat Commun. 2018;9:4613. 10.1038/s41467-018-06933-4.

3. Li Z, Chen S, Cui H, Li X, Chen D, Hao W, et al. Tenascin-C-mediated suppression of extracellular matrix adhesion force promotes entheseal new bone formation through activation of Hippo signalling in ankylosing spondylitis. Ann Rheum Dis. 2021;80:891–902. 10.1136/annrheumdis-2021-220002.
4. Chen S, Li Z, Chen D, Cui H, Wang J, Li Z, et al. Piezo1-mediated mechanotransduction promotes entheseal pathological new bone formation in ankylosing spondylitis. Ann Rheum Dis. 2023;82:533–45. 10.1136/ard-2022-223428.
5. Bridgewood C, Watad A, Russell T, Palmer TM, Marzo-Ortega H, Khan A, et al. Identification of myeloid cells in the human enthesis as the main source of local IL-23 production. Ann Rheum Dis. 2019;78:929–33. 10.1136/annrheumdis-2018-214944.
6. Cuthbert RJ, Watad A, Fragkakis EM, Dunsmuir R, Loughenbury P, Khan A, et al. Evidence that tissue resident human enthesis γδT-cells can produce IL-17A independently of IL-23R transcript expression. Ann Rheum Dis. 2019;78:1559–65. 10.1136/annrheumdis-2019-215210.
7. Altaie A, Simone D, McDermott N, Owston H, Attar M, Jin L, et al. Healthy human enthesis stromal cells mediate immunoregulation via the CD39/CD73 adenosine ectonucleotidase pathway. Ann Rheum Dis. 2025;84:1995–2007. 10.1016/j.ard.2025.09.001.
8. Wang X, Li F, Xie L, Crane J, Zhen G, Mishina Y, et al. Inhibition of overactive TGF-β attenuates progression of heterotopic ossification in mice. Nat Commun. 2018;9:551. 10.1038/s41467-018-02988-5.
9. Sorkin M, Huber AK, Hwang C, Carson WF, Menon R, Li J, et al. Regulation of heterotopic ossification by monocytes in a mouse model of aberrant wound healing. Nat Commun. 2020;11:722. 10.1038/s41467-019-14172-4.
10. Chen S, Lin Y, Yang H, Li Z, Li S, Chen D, et al. A CD26 + tendon stem progenitor cell population contributes to tendon repair and heterotopic ossification. Nat Commun. 2025;16:749. 10.1038/s41467-025-56112-5.
11. Sakaguchi N, Takahashi T, Hata H, Nomura T, Tagami T, Yamazaki S, et al. Altered thymic T-cell selection due to a mutation of the ZAP-70 gene causes autoimmune arthritis in mice. Nature. 2003;426:454–60. 10.1038/nature02119.
12. Ruutu M, Thomas G, Steck R, Degli-Esposti MA, Zinkernagel MS, Alexander K, et al. β-glucan triggers spondylarthritis and Crohn's disease-like ileitis in SKG mice. Arthritis Rheum. 2012;64:2211–22. 10.1002/art.34423.
13. Benham H, Rehaume LM, Hasnain SZ, Velasco J, Baillet AC, Ruutu M, et al. Interleukin-23 mediates the intestinal response to microbial β-1,3-glucan and the development of spondyloarthritis pathology in SKG mice. Arthritis Rheumatol. 2014;66:1755–67. 10.1002/art.38638.
14. Rehaume LM, Mondot S, Aguirre de Cárcer D, Velasco J, Benham H, Hasnain SZ, et al. ZAP-70 genotype disrupts the relationship between microbiota and host, leading to spondyloarthritis and ileitis in SKG mice. Arthritis Rheumatol. 2014;66:2780–92. 10.1002/art.38773.

15. Jo S, Lee SH, Park J, Nam B, Kim H, Youn J, et al. Platelet-Derived Growth Factor B Is a Key Element in the Pathological Bone Formation of Ankylosing Spondylitis. J Bone Min Res. 2023;38:300–12. 10.1002/jbmr.4751.
16. Nakamura A, Jo S, Nakamura S, Aparnathi MK, Boroojeni SF, Korshko M, et al. HIF-1α and MIF enhance neutrophil-driven type 3 immunity and chondrogenesis in a murine spondyloarthritis model. Cell Mol Immunol. 2024;21:770–86. 10.1038/s41423-024-01183-5.
17. Lee SH, Lee KH, Kim D, Jeon C, Whangbo M, Jo HR, et al. Targeting osteoclast-derived DPP4 alleviates inflammation-mediated ectopic bone formation in ankylosing spondylitis. Arthritis Res Ther. 2025;27:40. 10.1186/s13075-025-03474-2.
18. Percie du Sert N, Hurst V, Ahluwalia A, Alam S, Avey MT, Baker M, et al. The ARRIVE guidelines 2.0: Updated guidelines for reporting animal research. PLoS Biol. 2020;18:e3000410. 10.1371/journal.pbio.3000410.
19. Virtanen P, Gommers R, Oliphant TE, Haberland M, Reddy T, Cournapeau D, et al. SciPy 1.0: fundamental algorithms for scientific computing in Python. Nat Methods. 2020;17:261–72. 10.1038/s41592-019-0686-2.
20. Chen Y, Sun X, Su D, Luo F, Zhang M, Xu Y, et al. Posterior ligamentous injury induces progressive ankylosis-like structural remodeling in rhesus macaques. Biochem Biophys Res Commun. 2026;828:154089. 10.1016/j.bbrc.2026.154089.
21. Yu T, Zhang J, Zhu W, Wang X, Bai Y, Feng B, et al. Chondrogenesis mediates progression of ankylosing spondylitis through heterotopic ossification. Bone Res. 2021;9:19. 10.1038/s41413-021-00140-6.
22. Zhang D, Huang J, Sun X, Chen H, Huang S, Yang J, et al. Targeting local lymphatics to ameliorate heterotopic ossification via FGFR3-BMPR1a pathway. Nat Commun. 2021;12:4391. 10.1038/s41467-021-24643-2.
23. Lim DH, Lee EJ, Kwon OC, Hong S, Lee CK, Yoo B, et al. Effect of tumor necrosis factor inhibition on spinal inflammation and spinal ankylosis in SKG mice. Sci Rep. 2019;9:18000. 10.1038/s41598-019-54549-5.
24. Xie Z, Yu W, Zheng G, Li J, Cen S, Ye G, et al. TNF-α-mediated m6A modification of ELMO1 triggers directional migration of mesenchymal stem cell in ankylosing spondylitis. Nat Commun. 2021;12:5373. 10.1038/s41467-021-25710-4.
25. van Tok MN, Na S, Lao CR, Alvi M, Pots D, van de Sande MGH, et al. The Initiation, but Not the Persistence, of Experimental Spondyloarthritis Is Dependent on Interleukin-23 Signaling. Front Immunol. 2018;9:1550. 10.3389/fimmu.2018.01550.

Table

Table 1 Experimental groups and available assessments

Group	Intervention	n	Available assessments
Control	No pharmacological or surgical intervention	3	Monthly clinical/rotarod summaries; serial micro-CT images; endpoint regional micro-CT scores
Curdlan	3 mg i.p. on days 0 and 7	5	Clinical/rotarod summaries; imaging; terminal histology and serum; immunofluorescence
Structural injury	Posterior lumbar ligament complex injury at L2–L6	5	Clinical/rotarod summaries; imaging; terminal histology and serum; immunofluorescence

Terminal histology, serum, and immunofluorescence analyses compared the two intervention groups. SIJ immunofluorescence included four curdlan specimens and five structural injury specimens; posterior lumbar immunofluorescence included five specimens per group. Curdlan and structural injury animal identifiers were C1–C5 and AS1–AS5, respectively.

Figures

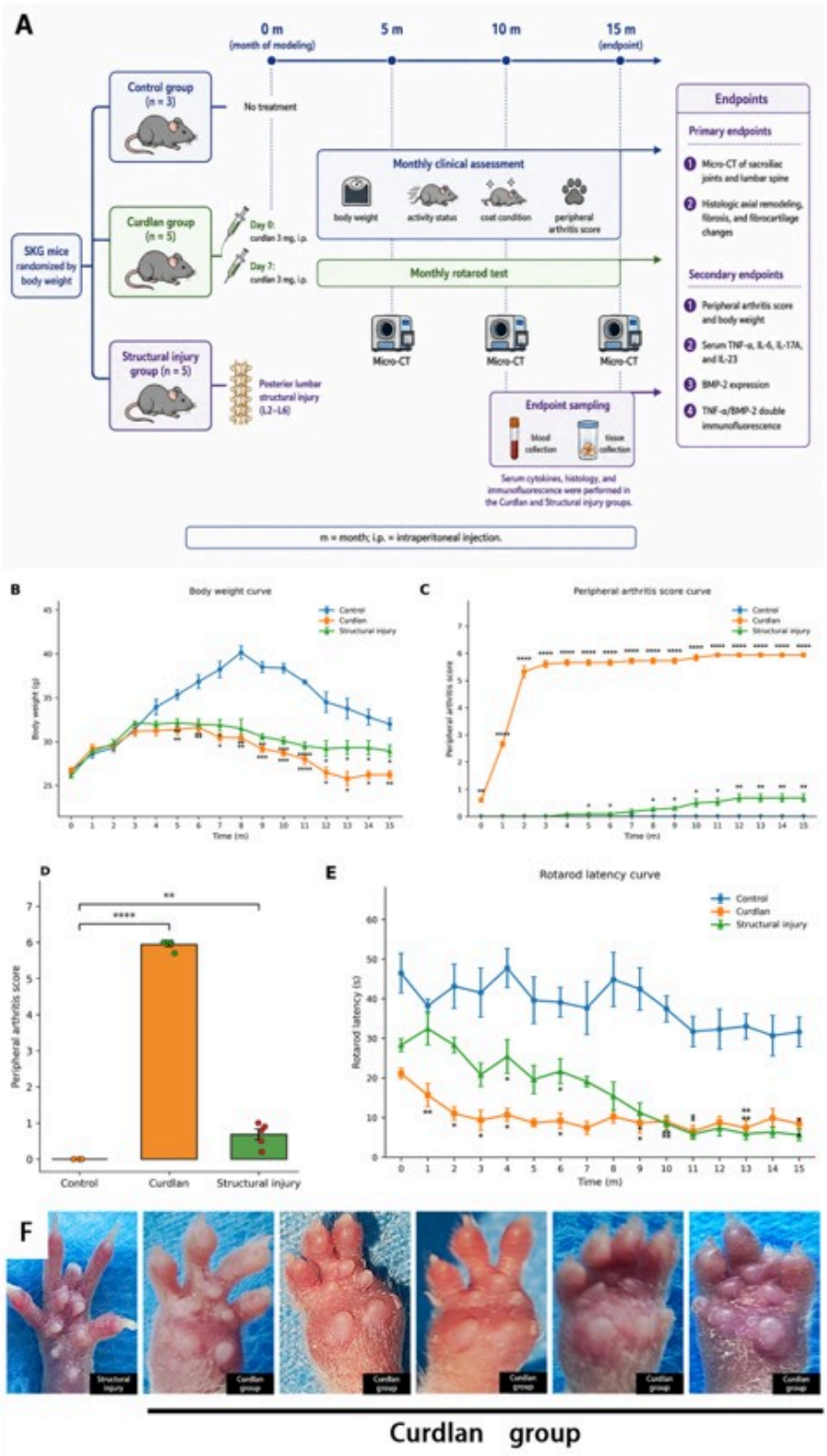


Figure 1

Longitudinal observations in the experimental groups

(A) Study timeline. (B–D) Body weight, peripheral arthritis score, and rotarod latency from month 0 to month 15. Values are group means ± standard error; Control n = 3, curdlan n = 5, and structural injury n =

5 at each tabulated time point. Trajectories are descriptive. Rotarod latency represents general motor performance and is not specific to axial function.

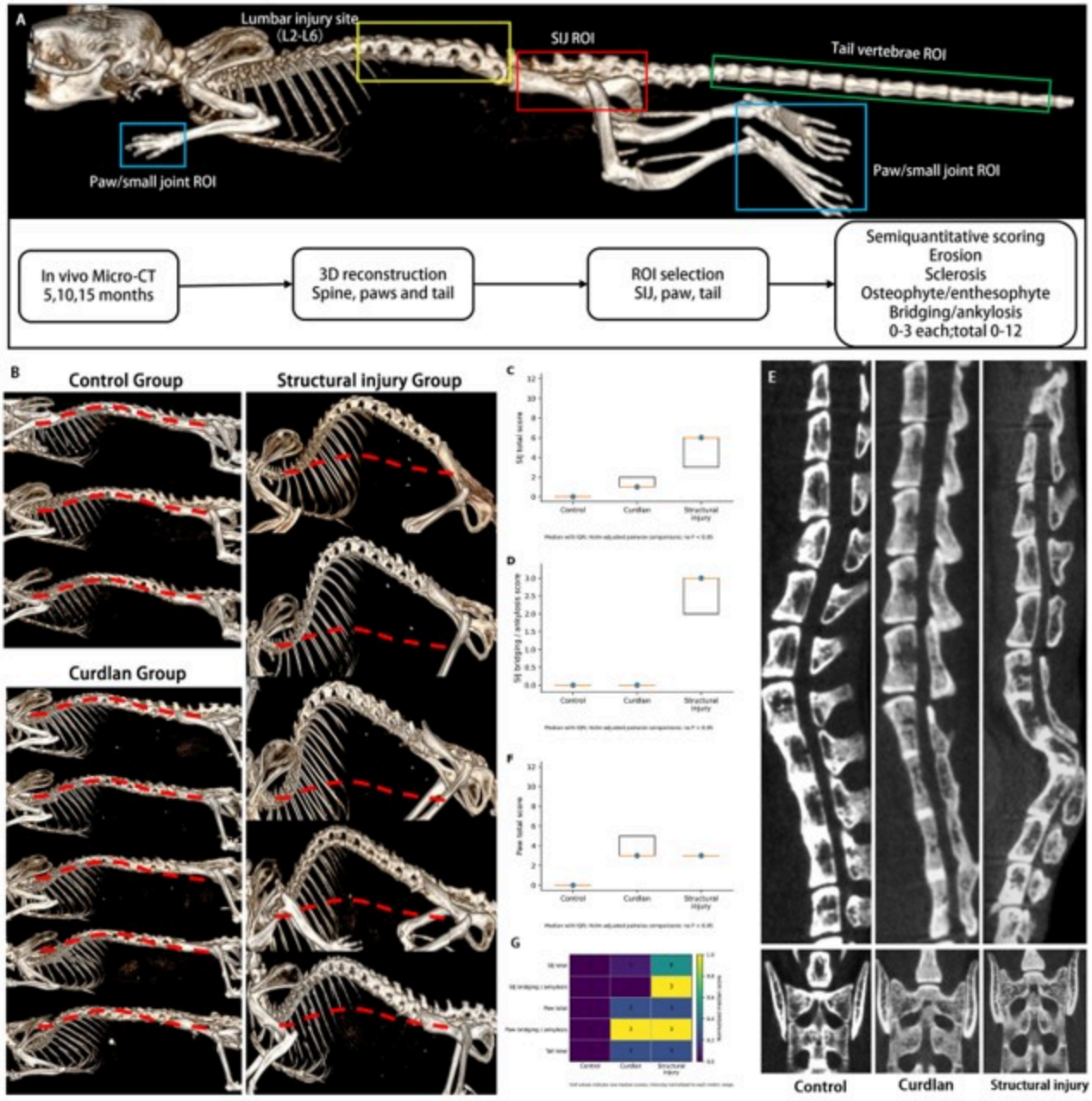


Figure 2

Anatomical imaging and endpoint regional scores

(A) Anatomical overview and scoring workflow. (B) Representative spinal reconstructions; dashed overlays provide qualitative alignment guides. (C) Representative spinal and SIJ multiplanar views. (D–F) Endpoint SIJ, paw, and tail total scores. Points represent individual animals; boxes indicate medians and interquartile ranges, with whiskers spanning the observed range. Control n = 3; curdlan and structural injury n = 5 each. No pairwise comparison reached significance after Holm adjustment within the corresponding region and endpoint.

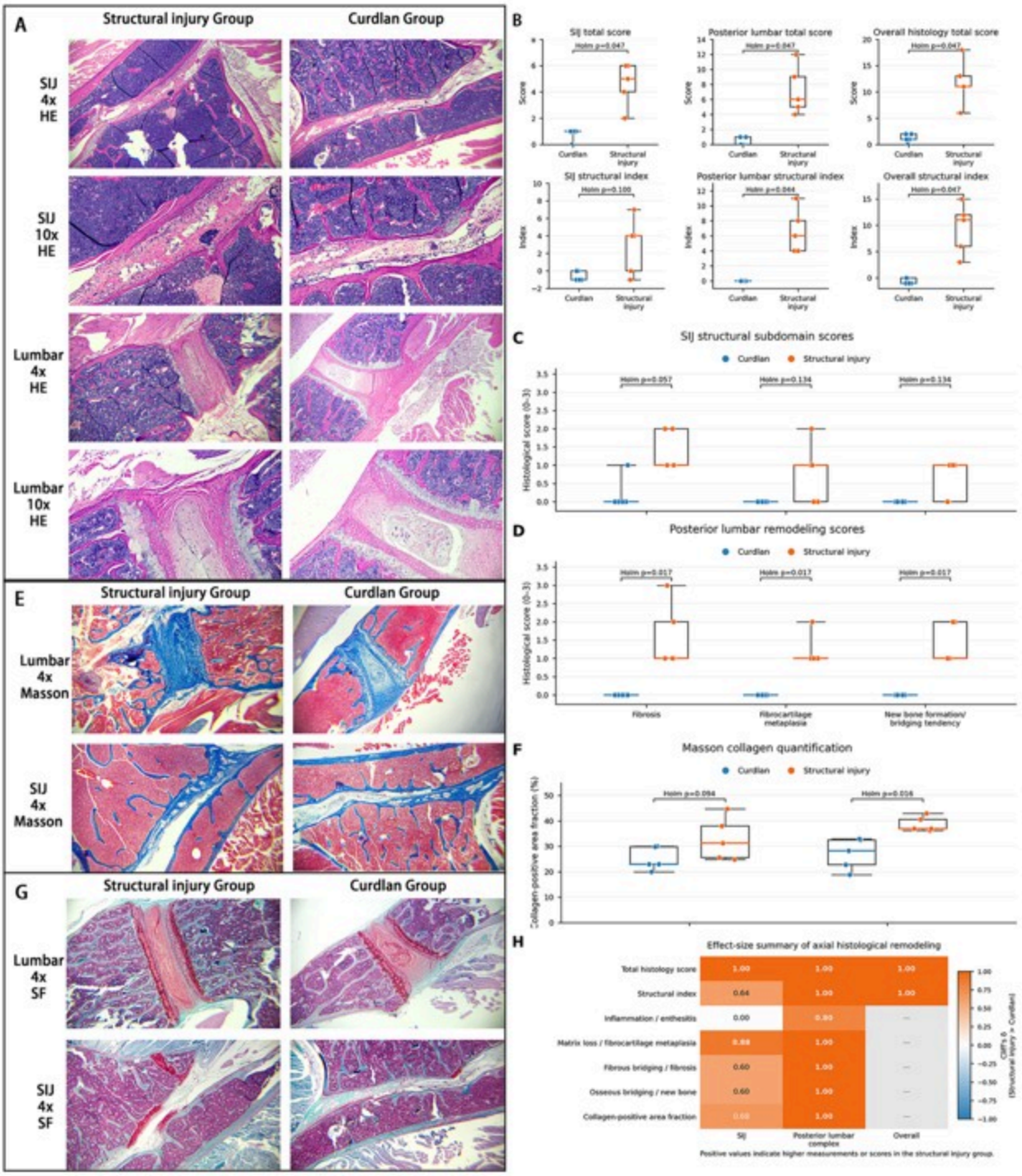


Figure 3

Terminal axial histology and collagen measurements

Representative H&E, Masson, and Safranin O/Fast Green panels are shown on the left, retaining the image-panel labels A, E, and G. (B) Six summary histology endpoints, adjusted as one family. (C) Posterior lumbar fibrosis, fibrocartilage metaplasia, and new bone/bridging-tendency scores, using correction across all five lumbar domains. (D) ROI-restricted collagen-positive area, adjusted across the two sites. Each point represents one animal (n = 5 per intervention group). Boxes show medians and

interquartile ranges with range whiskers; horizontal marks in dot plots denote medians. Scoring definitions and individual observations are provided in Tables S2–S3.

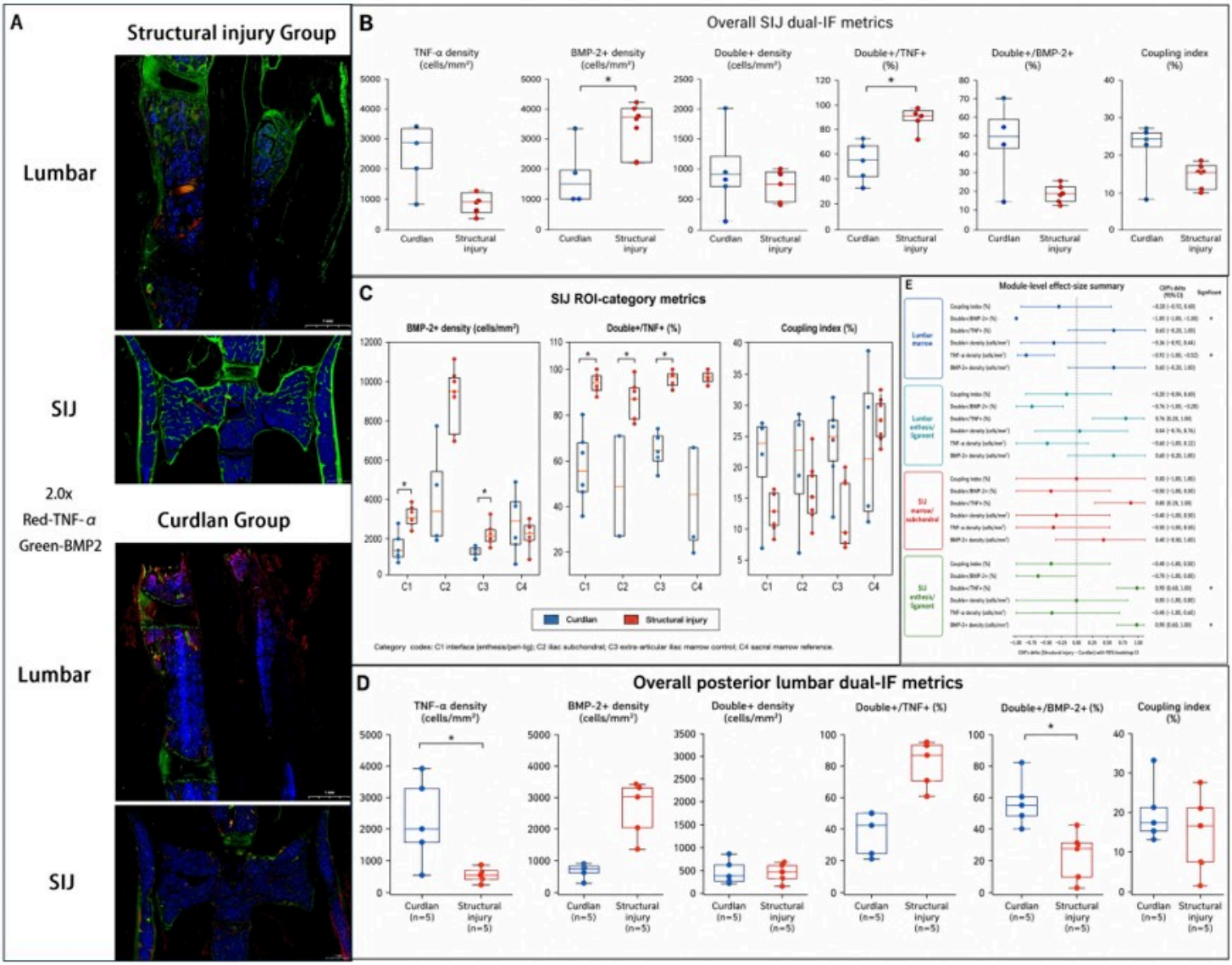


Figure 4

Exploratory TNF-α and BMP-2 immunofluorescence

(A) Representative posterior lumbar and SIJ sections stained for TNF-α (red) and BMP-2 (green), with nuclear counterstaining. (B) Overall SIJ densities. (C) Overall posterior lumbar densities. Overall values are unweighted means of nine ROIs per animal. SIJ: curdlan n = 4 and structural injury n = 5; posterior lumbar: n = 5 per group. Points represent animals; boxes indicate medians and interquartile ranges, with whiskers spanning the observed range. P values are nominal two-sided exhaustive permutation values without multiplicity adjustment. Positive signals indicate immunoreactivity and do not identify cell lineage.

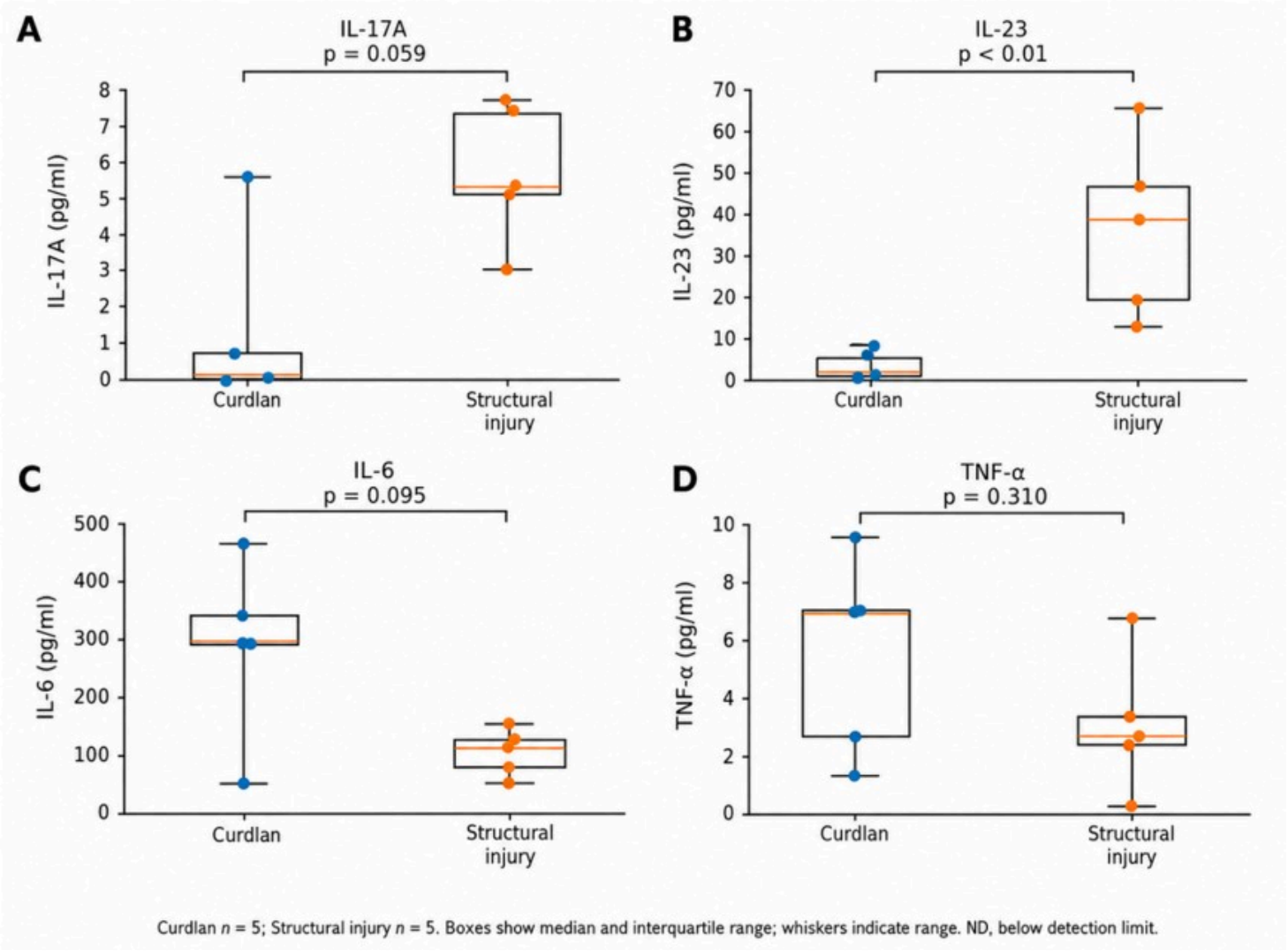


Figure 5

Terminal serum cytokines in the treated groups

(A–D) IL-17A, IL-23, IL-6, and TNF-α in the curdlan and structural injury groups (n = 5 each). Points represent animals; boxes show medians and interquartile ranges, with whiskers spanning the observed range. Two curdlan IL-17A observations were below detection and are displayed at the lower plotting boundary solely for visualization. P values are nominal two-sided exhaustive permutation values; no multiplicity correction was applied.

Supplementary Files

This is a list of supplementary files associated with this preprint. Click to download.

- 09Additionalfile2Supplementarytables.docx
- 10Additionalfile3Sourcedata.xlsx
- 08Additionalfile1Supplementaryfigures.docx